Wood Physics/Mechanical Properties

Sara Florisson*, Marie Hartwig, Malin Wohlert and Erik Kristofer Gamstedt

Microscopic computed tomography aided finite element modelling as a methodology to estimate hygroexpansion coefficients of wood: a case study on opposite and compression wood in softwood branches

https://doi.org/10.1515/hf-2023-0014
Received February 17, 2023; accepted July 12, 2023;
published online August 31, 2023

Abstract: Microscopic X-ray computed tomography (XμCT) aided finite element (FE) modelling is a popular method in material science to relate material properties to heterogeneous microstructures. Recently, a methodology was developed for the XμCT aided FE modelling of wood, which characterises the process from specimen preparation to estimation of material properties. In the current research, this methodology is tested on branches of Norway spruce (*Picea abies* (L.) Karst.) to estimate the hygroexpansion coefficients of opposite (OW) and compression wood (CW). These properties are largely unknown and have engineering implications. The study is complemented by measurements of density, moisture content (MC) and elastic moduli. Results showed that the methodology assisted in the design of an integrated process and the identification of bottlenecks. It was seen that the level of detail of the numerical model had a strong influence on the obtained hygroexpansion properties. CW from branches showed higher density and longitudinal shrinkage coefficients, and elastic moduli less affected by MC. These differences are unlikely caused by MC, but more likely by the characteristics of the microstructure.

Keywords: branches; calibration; digital volume correlation; hygroelastic properties; lab-based; Norway spruce

***Corresponding author: Sara Florisson**, Division of Applied Mechanics, Department of Material Science and Engineering, Uppsala University, Ångströmlaboratoriet, Lägerhyddsvägen 1, Uppsala 751 03, Sweden, E-mail: sara.florisson@angstrom.uu.se. https://orcid.org/0000-0001-7322-7052

Marie Hartwig, Malin Wohlert and Erik Kristofer Gamstedt, Division of Applied Mechanics, Department of Material Science and Engineering, Uppsala University, Ångströmlaboratoriet, Lägerhyddsvägen 1, Uppsala 751 03, Sweden. https://orcid.org/0000-0002-1620-6631 (M. Wohlert)

1 Introduction

1.1 XμCT aided FE modelling of wood

A state-of-the-art method to determine parameters for modelling comes from the field of bone and composite research and is called X-ray computed tomography (XμCT) aided finite element (FE) modelling (Auenhammer et al. 2022; Keyak et al. 1998). This method has only recently been applied to wood (Badel and Perre 2001; Florisson 2022; Fortino et al. 2017; Hachem et al. 2018; Huber et al. 2022; Kamke et al. 2014) and is complex and involves several steps. Most research on XμCT aided FE modelling focusses on certain steps that make up this process, which minimises the compatibility between image quality and model development (Auenhammer et al. 2021). An automatic transfer of information between different steps in this process is typically lacking. Non-automated, i.e. manual procedures, create labour intensive processes, as well as errors within and between each step of such a process that are larger than with an automated process (Florisson and Gamstedt unpublished data; Keyak et al. 1990). Recently, a methodology for XμCT aided FE modelling of wood was developed to promote a more efficient design and execution of this method (Florisson and Gamstedt unpublished data). The methodology focusses on wood with a moisture and temperature dependent material behaviour, but can also be used on other materials or material levels (μm – m). The methodology is presented in Figure 1 and consists of five different steps labelled *source*, *experiment*, *image processing*, *model development*, and *output*. The general principle of the methodology is that tomograms should be of quality that benefits the material characterisation, segmentation, fibre reconstruction, digital volume correlation (DVC), meshing and material model, where tomograms refer to the 3D reconstructed images (Withers et al. 2021). It is therefore important to

clearly state the aim and objective at the beginning of the XµCT aided FE process (Auenhammer et al. 2021). A detailed description of the methodology and its bottlenecks can be found in Florisson and Gamstedt (unpublished data).

1.2 Hygroexpansion in opposite wood and compression wood

In conifers, reaction wood is formed as compression wood (CW) in response to gravistimulus or external factors (Groover 2016). For instance, within the cross section of Norway spruce branches, the upper side consists of opposite wood (OW), what is known as normal wood (NW) in the stem, whereas the underside consists largely of CW (Timell 1986a,b,c). Compared to OW formed in branches of Radiata pine, CW differs in appearance, structure and properties. CW is recognised by its darker colour, and structurally by thicker tracheid walls, higher coarseness, larger microfibril angle (MFA), and higher wood density (Li et al. 2014). CW formed in the stem is also known to have a different chemical composition, having a higher lignification which is distributed over the entire tracheid wall, instead of being concentrated in the middle lamellae, as with OW (Nanayakkara et al. 2009; Timell 1986a; Zhang et al. 2016). CW found in branches and leaning stems show quite a difference in mechanical properties compared with the complementary OW or NW, respectively (Burgert et al. 2004; da Silva Moreira et al. 2023; Gonçalves et al. 2019; Guo et al. 2023; Marasigan et al. 2022; Müller et al. 2006; Stanzl-Tschegg et al. 2011), such as lower longitudinal stiffness. Research suggest that this is caused by the larger MFA of the cellulose strands in CW (Färber et al. 2001), however, its high lignification leads to comparable compression strength as in OW despite the MFA differences (Gindl 2002). The heterogeneity of wood, manifested by the presence of reaction wood, induces engineering challenges on the occasion of differential swelling and shrinkage due to moisture changes. CW found in branches of Scots pine shows a significant difference in longitudinal shrinkage compared to OW (Włoch 1975). Research suggests that this is due to the difference in chemical composition. In addition to the mentioned higher lignin content and different lignin distribution, a small proportion of highly swellable (1→3)-β-D-glucans is present in CW (Włoch 1975; Zhang et al. 2016). Both these components show significant shrinkage and swelling in isolated state. The chemical difference between CW in the stem, branch and seedlings is said to be similar (Nanayakkara et al. 2009). While reaction wood formed in trunks has been extensively investigated, relatively little has been reported on softwood branches. However, from a zero-waist perspective and an optimal use of material, the timber industry is looking for ways to use the entire tree in the production of engineered wood products rather than only stem wood (Hartwig and Gamstedt 2020; Olarescu et al. 2022). Therefore, a proper identification of the hygroexpansion properties of branch wood is needed. For a more general overview of reaction wood, please consider Groover (2016).

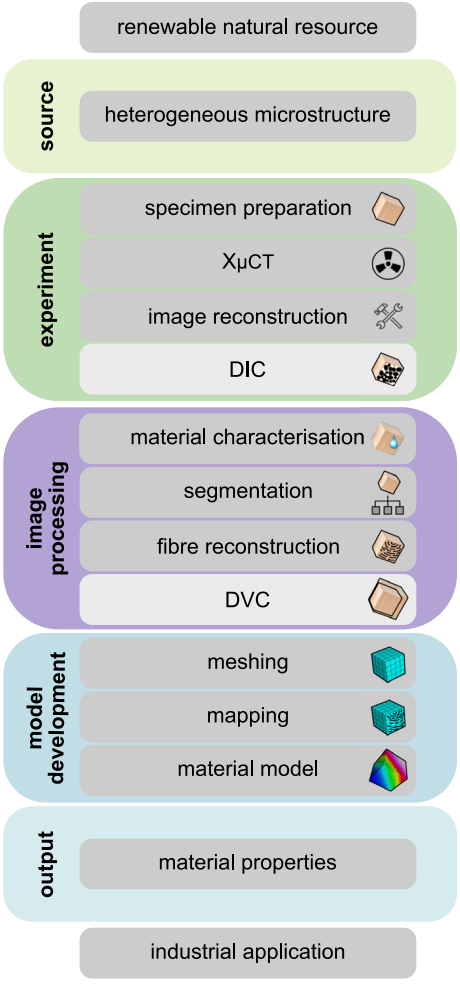

Figure 1: Methodology for the microscopic lab-based computed tomography (XµCT) aided finite element modelling of wood, where DIC indicates digital image correlation (2D) and DVC denotes digital volume correlation (3D) (Florisson and Gamstedt unpublished data).

1.3 Digital volume correlation

The calibration of an XµCT aided FE model is often supported by techniques such as DVC (Buljac et al. 2018; Forsberg et al. 2010; Hartig et al. 2021; Hild et al. 2016; Keunecke et al. 2012). Here, a calibration is the iterative fit between FE results and XµCT data in order to obtain material properties for modelling. DVC is an image-processing technique that can be

used to estimate the 3D displacement field of an object using a fixed image (reference tomogram) and a moving image (tomogram of the deformed object) (Bay et al. 1999). The technique knows a local and a global approach, where in the local approach, the tomograms get subdivided into small volumes, which are independently registered, and in the global approach, the entire moving image is mapped onto the fixed image, creating a continuous displacement field (Bay et al. 1999; Buljac et al. 2018; Madi et al. 2013). The mapping performed in the global approach is called image registration. Suitable registration methods for wood are affine and non-rigid (or elastic) registration, where affine registration is based on translation, rotation and scaling and non-rigid registration locally warps the image (Patera et al. 2018). To the authors knowledge, global DVC has not yet been used to analyse wood and its hygroexpansion coefficients.

1.4 Putting the methodology to test

The aim of the current paper is to test the recently developed XµCT aided FE methodology using a case study. The study focuses on the estimation of hygroexpansion properties of both OW and CW found in branches of Norway spruce. The FE model is developed using information from ex-situ hygroexpansion experiments performed with a XµCT scanner. Global DVC was adopted to obtain the displacement fields during testing, which were used to calibrate the numerical model.

2 Materials and methods

The research method used in the current study is visualised in Figure 2. The colour coding of the steps matches the colour coding of the steps making up the XµCT aided FE modelling methodology presented in Figure 1. The study consisted of (a) an experiment to study the hygroexpansion of OW and CW in branches of Norway spruce at 21 °C and 44 % and 98 % relative humidity (RH) using an ex-situ XµCT approach, (b) a DVC analysis to determine the 3D displacement fields of OW and CW during hygroexpansion from tomograms obtained in step (a), (c) a FE model to simulate the hygroexpansion of OW and CW under the same environmental conditions, and (d) a calibration of the FE model based on the DVC results to obtain the hygroexpansion coefficients related to the local *l*, *r*, and *t* material directions of OW and CW. Ex-situ indicates that the climatisation is performed outside of the scanner. In step (a) compression tests are used to determine the elastic moduli related to the main axes of the global coordinates system (*x*, *y* and *z*) at both 44 % and 98 % RH. In addition, the gravimetric moisture content (MC) and dry density of each specimen was estimated at the end of step (a). The results from the compression test were used to establish a relationship between the obtained elastic moduli and the MC for modelling purposes.

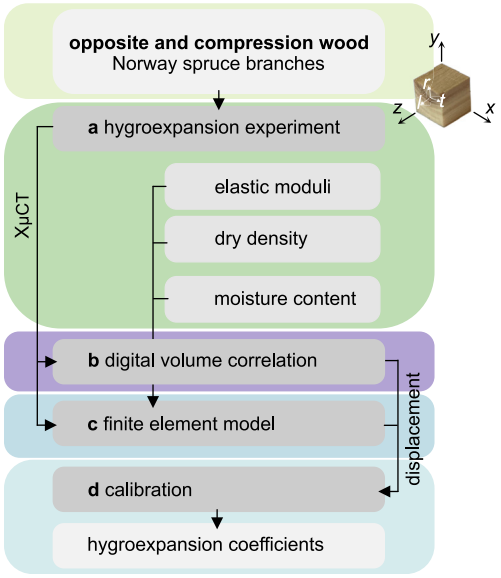

Figure 2: Method used to estimate the hygroexpansion coefficients of opposite and compression wood found in Norway spruce branches. The colour coding of the steps matches colour coding of the steps making up the microscopic lab-based computed tomography (XµCT) aided finite element modelling methodology presented in Figure 1. Also, an indication of the local (*l*, *r* and *t*) and global (*x*, *y*, *z*) coordinate systems is given.

2.1 Experiments

2.1.1 Specimen preparation: Branches of Norway spruce were retrieved from Tranås in Småland county in Sweden. The branches were labelled A1, A2, B1, B2, B3 and B4, where A and B indicated a different fan of branches. After felling, the branches were labelled, wrapped in plastic and kept under frozen conditions before being cut into specimens as seen in Figure 3 by a professional carpenter. During the cutting process, the specimens had the possibility to dry. In total 18 specimens of OW and 18 specimens of CW were obtained for testing. The selection procedure resulted in three OW specimens and three CW specimens per branch, which were numbered according to Figure 3a and were located as close to the stem as possible. The nominal cross-sectional dimensions of the specimens were $5 \times 5 \times 5$ mm^3. All 36 specimens were tested as part of the experiment. One randomly chosen OW specimen (B4-OW-1) and one matching CW specimen (B4-CW-1) were used in the DVC analysis and FE simulations.

2.1.2 Test setup

2.1.2.1 Computed tomography: A SkyScan 1172 XµCT scanner (Bruker, Belgium) (see Figure 4a and b) was used to obtain tomograms of the 36 OW and CW specimens. The scanner was equipped with a filament, electromagnetic lens, target, scintillator, specimen stand and an image detector. The X-ray source, which produced a cone beam, and the detector were positioned on opposite sides of specimen stand, see Figure 4b and c. The stand rotated during scanning and has the possibility to change its position between the source and the detector. This allows scanning of different specimen sizes. The SkyScan NRecon reconstruction software was used to reconstruct the cross-sectional slices obtained from angular projections during XµCT scanning

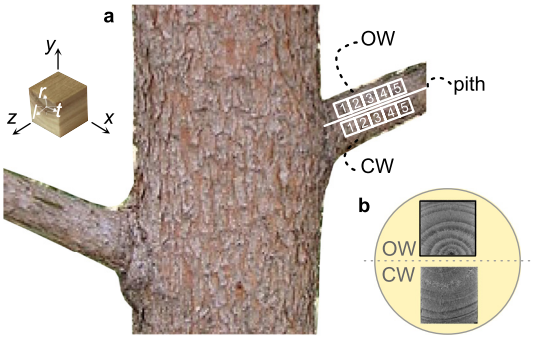

Figure 3: Location of the opposite wood (OW) and compression wood (CW) specimens within the tree branch: (a) the location within the branch and (b) the location within the cross section of the branch. Also, an indication of the local (*l*, *r* and *t*) and global (*x*, *y*, *z*) coordinate systems is given.

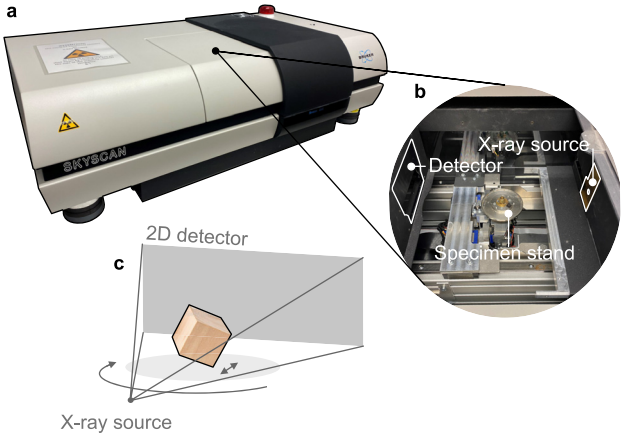

Figure 4: Computed tomography scanner: (a) SkyScan 1172 XμCT scanner, (b) inside of scanner showing the detector, X-ray source, and specimen stand, and (c) graphical illustration of the 2D detector, cone beam X-ray, and specimen on holder.

(SkyScan 2011). The software used a modified Feldkamp algorithm with automatic adaption for the reconstruction.

2.1.2.2 Compression tests: A Shimadzu Autograph AGS-X universal testing machine (UTM: Shimadzu, Tokyo, Japan) was used to perform compression tests. The UTM was equipped with a 500 N load cell. The force-displacement curve was obtained with a TRViewX Shimadzu Digital Video Extensometer (Shimadzu, Tokyo, Japan), which is a non-contact extensometer. The compression test setup prevented sideways lateral contact slipping caused by Poisson effects. This causes shear stress to develop close to the loading plates. The loading plates are in a fixed position and not allowed to rotate, which can result in uneven compression of specimens with non-parallel contact surfaces. In addition, the non-contact extensometer measured the displacement of the loading plates instead of the displacement of the specimen. This was done due to the small dimensions of specimens and leads to average values of displacement rather than local measurements. These design choices can lead to small errors when it comes to the determined elastic moduli. It was assumed that any machine compliance did not influence the deformation measurements of the wood specimens.

2.1.3 Experimental procedure

2.1.3.1 Conditioning: The specimens were conditioned in a desiccator at 44 and 98 % RH. Potassium carbonate was used to create a RH of 44 % at room temperature (21 °C). This corresponded to an ideal MC of 10 % for wood (Simpson 1971). Potassium sulphate was used to create a RH of 98 % at room temperature. This corresponds to an ideal MC of 25 % (Simpson 1971). During conditioning, the desiccator remained closed. The climate inside the desiccator was tracked with a temperature and RH data logger of type Intab Comet Q-U3120 (±0.4 °C and ±1.8 % RH) (COMET system, Rožnov pod Radhoštěm, Czech Republic). This logger had a temperature range between −30 °C and +70 °C and a RH range between 0 % and 100 %. Pre-testing done on a dummy specimen showed that 72 h was sufficient to reach equilibrium MC using two measuring points a day. No signs of mould growth were observed within this time period.

2.1.3.2 Computed tomography: The XμCT scanner was used to obtain tomograms of the OW and CW sample sets after conditioning at 44 % RH and after conditioning at 98 % RH. This means that *ex-situ* testing was used. During scanning the specimens were wrapped in polyethylene household wrap. The temperature inside the scanner was 26–27 °C during scanning. The scanner used the standard flatfield correction technique (bright and darkfield) during each scan to improve the quality of the tomogram. A flatfield correction accounts for the non-uniform illumination of the detector by the polychromatic X-ray beam and the sensitivity variation of pixels by acquiring a projection without the specimen inside the field of view (Withers et al. 2021). The settings that were used for scanning can be found in Table 1. For a thorough explanation of the effect of each scanning parameter on image quality, Zwanenburg et al. (2022) can be consulted.

The reconstruction of the tomograms consisted of a ring artefact reduction and defect pixel masking. The tomograms of the specimens B4-OW-1 and B4-CW-1 used for DVC and FE modelling were also cropped and rotated. The settings for these two specimens are collected in Table 2. Although these settings are software specific, the values have been presented for the purpose of reproducibility. In du Plessis et al. (2020), the effect of these settings on image quality can be found. The chosen intensity range for each image was 0–0.16. Each projection was digitised to an 8-bit image (TIFF greyscale format).

Table 1: XμCT scanning settings.

Variable	Setting
Voxel size	2.99 μm
Voltage	49 kV
Current	200 μA
Exposure time	750 ms
Frame averaging	4
Filter	–
Rotation increment	0.2°
Rotation	180°
Scanning time	~6 h
Temperature	26–27 °C

Table 2: Reconstruction settings.

	B4-CW-1-44	B4-CW-1-98	B4-OW-1-44	B4-OW-1-98
Image size given in number	1732	1756	1768	1756
of voxels (*x*, *y*, *z*)	1716	1748	1716	1776
	1696	1776	1736	1816
Defect pixel masking (%, severe)	3	3	3	3
Alignment optimization (automatic)	28	30	31.5	26
Ring artefact correction	50	50	50	50
Cross-sectional rotation	4°	−1°	11°	5°

2.1.3.3 Compression test: The compression tests were performed on all 36 specimens in the OW and CW sample sets. The tests were executed displacement-controlled with a displacement rate of 0.5 mm/min. The sampling rate was 100 Hz. A load limit was set to prevent plastic deformations. The load limits were based on pre-tests made on dummy specimens. For the *x* and *y* direction, the limit was set to 50 N. For the *z* direction, the limit was set to 250 N. For directions see Figure 2. The displacement schedule consisted of one step, without an unloading step. The elastic moduli were determined according to

$$E_i = \frac{\Delta F}{\Delta a}\frac{x_i}{A} \tag{1}$$

where E is the elastic modulus, i indicates the loading direction (x, y, z), ΔF is the regarded section of the force curve, x_i is the length of the cube corresponding to the chosen loading direction, Δa is the regarded section of the displacement curve, and A is the cross-sectional area of the loaded surface. ΔF was chosen 30–40 N for the x and y direction and 150–200 N for the z direction. These ranges were shown to be clearly within the elastic linear regime. The noise was removed from the force-displacement data with MATLAB® (MathWorks, Natick, United States) statement '*movmean*' considering a range of 100 data points.

2.1.3.4 Oven-dry density: The oven-dry density, ρ_0, of each specimen in the OW and CW sample sets was determined according to

$$\rho_0 = \frac{m_0}{V_0} \tag{2}$$

where m_0 is the oven-dry mass and V_0 is the oven-dry volume of the specimen. The oven-dry mass was determined by drying the specimens in an oven at 103 °C ± 2 °C (European Committee for Standardization 2003). The mass of each specimen was measured with a Mettler Toledo scale XS105 ±0.01 mg that has a range of 15 mg–820 g (Mettler Toledo, Columbus, USA). The dimensions of the specimen were measured with a Cocraft 40–8747 Digital Calliper ±0.03 mm that has a 150 mm range (Clas Ohlson, Insjön, Sweden).

2.2 Finite element model

A 3D numerical model was created in commercial software Abaqus FEA® (SIMULIA 2017b). The model was used to simulate the hygroexpansion of specimens B4-OW-1 and B4-CW-1. The material model was implemented in user-subroutine UMAT (SIMULIA 2017a). The orthotropic material orientation was defined in user-subroutine ORIENT as a local material orientation. The FE model was kept relatively simple, since the aim of the case study is to test the proposed methodology rather than giving a detailed analysis of wood. This means that the material is assumed homogeneous, and no distinction is made in density differences due to latewood, transition wood and earlywood. Also, no moisture gradients are assumed in the wood's volume, eliminating mechanosorption from the analysis.

2.2.1 Theory: The constitutive relation for the stress rate, $\dot{\overline{\boldsymbol{\sigma}}}$, used to describe the elastic and hygroexpansion behaviour of wood is given as

$$\dot{\overline{\boldsymbol{\sigma}}} = \overline{\mathbf{C}}^{-1}\left(\dot{\overline{\boldsymbol{\varepsilon}}} - \dot{\overline{\mathbf{C}}}\overline{\boldsymbol{\sigma}} - \dot{\overline{\boldsymbol{\varepsilon}}}_h\right) \tag{3}$$

where the total strain rate, $\dot{\overline{\boldsymbol{\varepsilon}}}$, the elastic strain rate, $\dot{\overline{\boldsymbol{\varepsilon}}}_e$, and the strain rate due to hygroexpansion, $\dot{\overline{\boldsymbol{\varepsilon}}}_h$, are given by

$$\dot{\overline{\boldsymbol{\varepsilon}}} = \dot{\overline{\boldsymbol{\varepsilon}}}_e + \dot{\overline{\boldsymbol{\varepsilon}}}_h \tag{4}$$

$$\dot{\overline{\boldsymbol{\varepsilon}}}_e = \overline{\mathbf{C}}\dot{\overline{\boldsymbol{\sigma}}} + \dot{\overline{\mathbf{C}}}\overline{\boldsymbol{\sigma}} \tag{5}$$

$$\dot{\overline{\boldsymbol{\varepsilon}}}_h = \boldsymbol{\alpha}\dot{w}_a \tag{6}$$

and where $\mathbf{C}$ is the compliance matrix, $\boldsymbol{\alpha}$ is a matrix that contains the hygroexpansion coefficients in the main orthotropic directions l, r, and t, $\dot{w}_a$ is the moisture content rate below fibre saturation point, and $(\dot{\bullet})$ indicates the local material orientation. An elaborate description of the theory and its implementation into FE modelling can be found in Ormarsson (1999).

2.2.2 Specifications FE model: The meshed geometry of the numerical model is presented in Figure 5a. The dimensions are based on the mean height, width and length of each OW and CW sample set measured inside the tomograms obtained at 44 % RH as part of the experiment. The values can be found in the SI section "Parameters for modelling". A structured linear hexahedral mesh was used. A mesh refinement was performed based on the displacement results, where computational time was the limiting factor. The chosen mesh size was 0.2 mm. The cube is supported by four pinned supports as visualised in Figure 5a, where the circle in the centre of the cube shows the fourth support fixed in x, y and z direction and located at the bottom of the cube in the far back. The support on the left is fixed in x and y direction, whereas the other two supports are fixed in only y direction. The cube will be subjected to a RH change from 44 to 98 %. The model assumes this change as a linear change in the MC pf the cube in time, which occurs uniformly over the entire volume. This means that no moisture gradients will occur during wetting. The MCs are a mean value of each OW and CW sample set measured as part of the experiment. The values are presented in Section 3.3.

The location of the pith in the global coordinate system (x, y, z) both at the front ($p_{2,x}$, $p_{2,y}$) and the back ($p_{1,x}$, $p_{1,y}$) of the B4-OW-1 and B4-CW-1 specimen at 44 % RH is needed to define the local coordinate system that describes the annual ring curvature for each specimen. The information is used in user-subroutine ORIENT to establish a local coordinate system (l, r, t). The method to determine the pith location in the x–y plane is visualised in Figure 5b. The locations were retrieved from the tomograms by manually drawing circles along the annual rings using commercial software Avizo™ 3D 2021.2. The centres of these circles were assumed to coincide with the pith. The subroutine draws a line between points $p_{1,x}$ and $p_{2,x}$. The values obtained for the pith location are collected in the SI section. The locations were used to establish the local material orientation with user-subroutine ORIENT (SIMULIA 2017a).

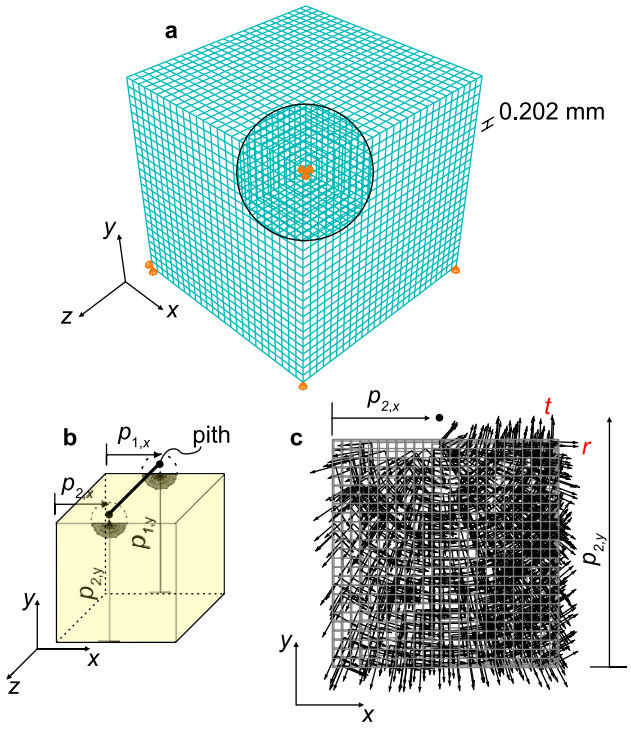

Figure 5: Specifications model. (a) Geometry and boundary conditions model, (b) visualisation method for pith detection, and (c) visualisation of the orthotropic material orientation constructed by the numerical model.

The elastic moduli related to the *l*, *r* and *t* material direction will be described using

$$E_l = E_{l0} + E_{lw}(w_f - w_a) \quad (7)$$
$$E_r = E_{r0} + E_{rw}(w_f - w_a) \quad (8)$$
$$E_t = E_{t0} + E_{tw}(w_f - w_a) \quad (9)$$
$$w_f = 0.3(1 + 0.003(20 - T)) \quad (10)$$

where, E_{l0} is a reference value, E_{lw} indicates the linear dependency of the elastic modulus on MC, w_f is fibre saturation point and can be determined with Equation (10), w_a indicates the MC below fibre saturation point, and T is temperature in degrees Celsius (Florisson et al. 2021). The values of E_{l0} and E_{lw} will be determined with the results from the compression tests and a linear regression analysis performed in the Curve Fitter application provided by MATLAB® using Custom Equation. The results are collected both in Section 3.3. The Poisson ratios and the MC and temperature dependent shear moduli are taken from Florisson et al. (2021). The values for each cube and RH level are collected in Table 3. The hygroexpansion coefficients related to the *l*, *r*, and *t* material direction are obtained with a calibration of the FE model based on DVC results. More details on this procedure can be found in Section 2.4.

2.3 Digital volume correlation

A global DVC analysis was performed to obtain the 3D displacement fields caused by swelling directly from tomograms. The DVC analysis was performed in commercial software Avizo™ 3D 2021.2 (AVIZO 2021). The solution technique behind global DVC can be described as

Table 3: Material properties at 44 % and 98 % relative humidity for modelling specimens B4-OW and B4-CW, where *G* is the shear modulus at 21 °C and *v* is the Poisson ratio, and *l*, *r*, and *t* indicate the local material directions.

	B4-OW-44	B4-OW-98	B4-CW-44	B4-CW-98
G_{lr} (MPa)	666	516	666	516
G_{lt} (MPa)	632	482	632	482
G_{rt} (MPa)	52	48	52	48
v_{lr} (–)	0.35	0.35	0.35	0.35
v_{lt} (–)	0.60	0.60	0.60	0.60
v_{rt} (–)	0.55	0.55	0.55	0.55

$$f(x) = g(x + u(x)) \quad (11)$$

where, *f* refers – in the current study – to the reference tomogram (fixed image) at 44 % RH and *g* refers to the deformed tomogram (moving image) at 98 % RH. The position vectors are indicated by *x* and the sought displacement field by *u*. Solving Equation (11) is equivalent to minimising the correlation residual $\eta = f - g$, which should be close to the imaging noise level (AVIZO 2021). The problem can be linearized and expressed as a matrix inversion problem

$$\mathbf{M}\delta\mathbf{u} = \mathbf{b} \quad (12)$$

where $\mathbf{M}$ is the problem matrix, $\delta\mathbf{u}$ is the sought increment of displacement at the considered increment, $\mathbf{b}$ depends on the image gradient of *f* and residual η. Since $\mathbf{M}$ is constant, the solution consists of successive updates of $\mathbf{b}$ after each iteration. The algorithm converges when the displacement increment norm $|\delta\mathbf{u}|$ is smaller than the tolerance set by the user, and indicates that a desired solution for the displacement field $u(x)$ is found. The algorithm stops when it has converged or if the maximum number of iterations is reached. The algorithm implemented in global DVC uses affine registration to align the fixed image and moving image for analysis. An affine transformation captures translation, rotation, scaling and shear. It uses global transformation, which indicates that a single equation is used to register the entire image. Affine registration is suitable to capture the heterogeneous deformations of wood (Patera et al. 2018). A detailed description of the global DVC algorithm can be found in Madi et al. (2013).

The initial displacement field needed for the global DVC analysis came from a local DVC analysis. The settings used to perform both calculations are collected in Table 4. The sub-volume size and mesh size, as well as the convergence criterion of the global analysis, were chosen based on a refinement study. The correlation threshold, which discards bad measurements, was also chosen with a refinement study. Manual measurements of displacement were used to validate the global DVC analyses. The measurements were also made in commercial software Avizo™ 3D 2021. For each primary direction (*x*, *y* and *z*), 10 manual measurements were made along the chosen direction using a spacing of 0.5 mm for every selected tomogram slice with also a spacing of 0.5 mm. The results of this validation can be found in the SI section.

2.4 Calibration

The hygroexpansion coefficients in the *l*, *r*, and *t* material direction for specimens B4-OW and B4-CW were determined with an iterative fit

Table 4: Local and global digital volume correlation (DVC) analysis settings.

Local DVC		
	B4-OW	**B4-CW**
Sub-volume size (μm)	0.5	0.5
Max. displacement (mm)	0.125	0.125
Standard of measurement	Correlation	Correlation
Correlation threshold	0.5	0.5
Analysis	Translation	Translation
	Rotation	Rotation
	Shear	Shear
Global DVC		
	B4-OW	**B4-CW**
Mesh size (μm)	0.2	0.2
Convergence tolerance (nm)	2	1
Max. iterations	945	513

between numerical and DVC displacement data related to the x, y, and z direction. The fit was evaluated by computing the mean squared error (MSE) between the FE and DVC dataset. This was done in MATLAB® using statement '*immse*'. The best fit was determined by the smallest MSE for all three orthotropic material directions.

3 Results and discussion

This section presents the key findings of a case study used to assess the XμCT aided FE process of wood to determine the hygroexpansion coefficients of OW and CW in branches of Norway spruce. The coefficients have not been estimated with such precision before. Above the hygroexpansion oefficients, this section also presents the elastic moduli for OW and CW. A relation between elastic moduli and MC and between elastic moduli and dry density are established, and a reflection of the XμCT aided FE process is given.

3.1 Evaluation methodology

The XμCT aided FE process used in this study considered the following steps: specimen preparation, XμCT scanning, reconstruction, orthotropic material orientation, DVC, material model and prediction of material properties. In this section the bottlenecks observed within each step are discussed. The process is optimal when the *experimental* step is designed and executed to benefit the *image processing* and *model development* step. In the specimen preparation step, the specimens were brought to a constant MC with desiccators and covered in plastic to maintain this MC thorough scanning. The plastic coverage prevented motion artefacts from occurring in the tomograms, but resulted in a tedious DVC pre-processing. The specimens were tested in the XμCT scanning step using an *ex-situ* scanning approach. This approach led to rotational and translational misalignment between tomograms, which had to be manually undone. To automate the process and obtain higher quality tomograms, an *in-situ* scanning approach is recommended using a built-in climate chamber to the scanner. A visible artefact that was present inside the tomograms was ring artefacts. The dead pixels in the detectors resulted in ring artefacts during reconstruction, of which some could be removed through image processing. Such artefact negatively influences DVC (Limodin et al. 2011). In the material orientation step the pith detection was estimated manually using the structure of the annual rings. This detection can also be done automatically by using a Hough transformation (Huber et al. 2022). This method can be combined with an estimation of the local material orientation (l, r, t) using a gradient structure tensor. In the DVC step it was noticed that an appropriate *spatial* and *contrast* resolution is essential for DVC, since the tomograms need a recognisable random pattern for the analysis to converge. Both DVC analyses were successful, but it could be seen that the CW tomograms, with a higher level of contrast, led to an easier convergence (less iterations, smaller tolerance) and a smaller difference between manual and DVC measurements. Since the scanner does not run a warm up scan, the DVC measurements might be affected by thermal drift of the X-ray emission point (Wang et al. 2017). In the model development step, the assumption was made that the material is homogeneous, in the sense that no distinction between early, late and transition wood exists. Also, a linear change in MC was assumed, leading to an absence of moisture gradients within the volume during drying. This simplifies the displacements computed by the FE model. In general, it can be said that the *estimation of hygroelastic properties* is possible with the proposed methodology. However, the results showed that the accuracy of the properties is largely dependent on the level of detail of the model. Comparison with estimates using a more detailed numerical model is therefore warranted.

3.2 Hygroexpansion coefficient

In this study, we have tested the presented methodology on one specimen of OW and one of CW as a proof of concept to precisely determine hygroexpansion coefficients of OW and CW in their principal material directions – longitudinal, radial and tangential. The sample size is not large (number specimens) and differs (number branches, trees) enough to represent the variability of material. Therefore, more tests

Table 5: Hygroexpansion coefficient, α, for the opposite wood (OW) and compression wood (CW) specimen, where l, r, and t indicate the local material orientations and MSE is the mean squared error.

	α_l (–)	MSE	α_r (–)	MSE	α_t (–)	MSE
OW	–0.004	$2.66{\cdot}10^{-4}$	0.27	$5.00{\cdot}10^{-4}$	0.17	$6.70{\cdot}10^{-4}$
CW	0.19	$1.77{\cdot}10^{-4}$	0.25	$2.37{\cdot}10^{-4}$	0.15	$2.01{\cdot}10^{-4}$

are required in the future to be able to draw statistically significant conclusions. The obtained hygroexpansion coefficients are collected in Table 5. It should be noted that these coefficients were all obtained from FE models built from tomographic data. The table also presents the error (MSE) at which the calibration of the FE model was accepted. Figure 6 shows the displacement data at which the error was smallest, together with colour plots from FE and DVC analyses.

The longitudinal hygroexpansion coefficient of OW is considerably smaller than the coefficient for CW. This observation was also made by Włoch (1975) for specimens of branch wood from Spruce pine. The hygroexpansion coefficient for OW found in this study is negative. This indicates a decrease in length during moisture uptake. Such a decrease was also reported by Burgert et al. (2007) for specimens of Norway spruce NW analysed at the micro level. Perstorper et al. (2001) found an average value of 0.00773 (–) for Norway spruce NW and 0.021 (–) for Norway spruce CW from stem.

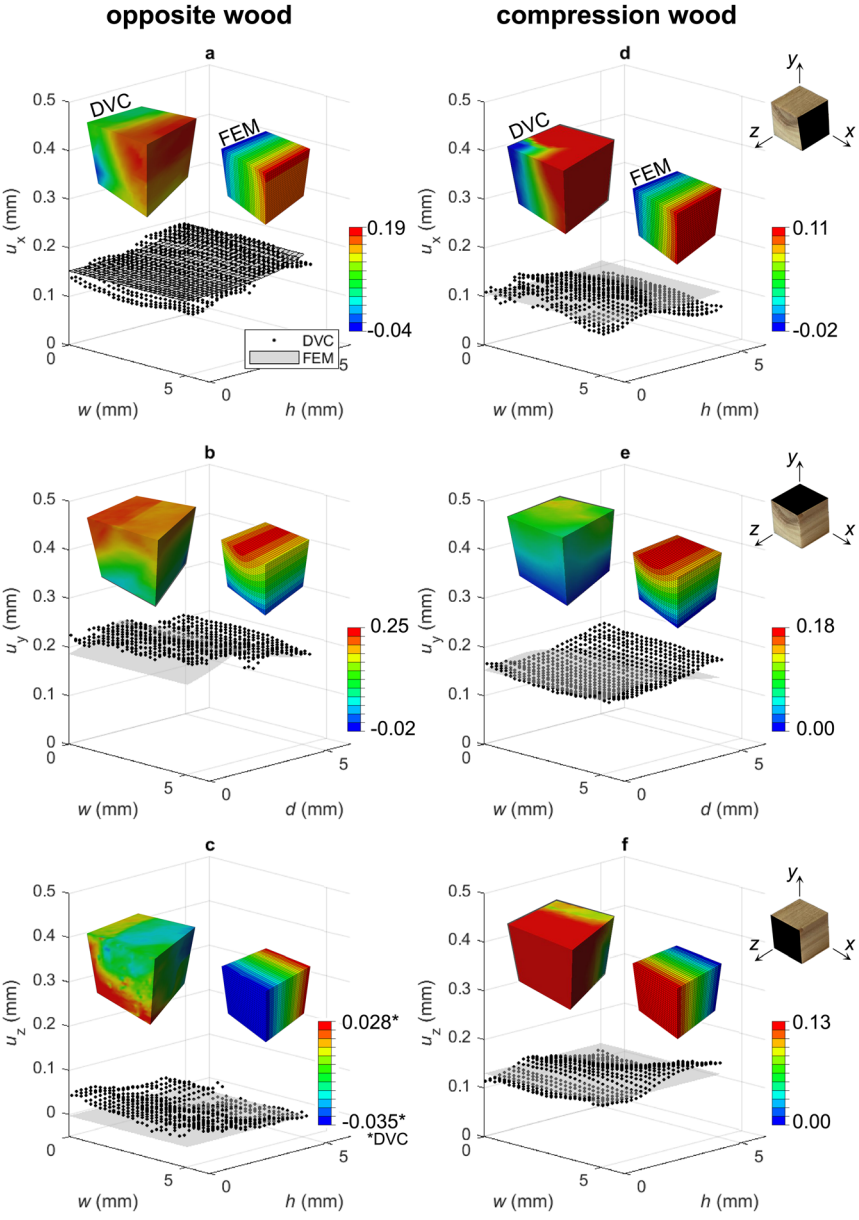

Figure 6: Displacement data from finite element (FE) and digital volume correlation (DVC) analyses for opposite and compression wood in principal material directions x, y, and z, with corresponding colour plots. Also, an indication of the global coordinate system is given, together with an indication of analysed surface (black). Displacement in principal material directions x, y, and z from finite element (FE) simulation and DVC analysis for opposite and compression wood.

The hygroexpansion coefficient for CW found in this study is much larger than reported by Perstorper et al. (2001) for stem wood.

The transverse hygroexpansion coefficients found in this study only show small differences between OW and CW, with slightly higher values for OW. Perstorper et al. (2001) reported an average radial hygroexpansion coefficient for Norway spruce NW of 0.151 (–) and for CW from stem a value of 0.105 (–). For the tangential hygroexpansion coefficient, an average value of 0.334 (–) was found for NW and 0.242 (–) for CW from stem. Our results are also in agreement with the bulk results published by Lanvermann et al. (2014). However, the tangential values found in this study are unexpectedly higher than the radial values. The most likely explanation for this difference is the simple nature of the FE model. The model assumes the material as homogeneous in the sense that is makes no distinction between early, late and transition wood. It also neglects moisture gradients within the volume during drying. This simplifies the interpretation of material behaviour. In reality, a moisture gradient will arise during adsorption, which will create an internal constraint due to differential swelling over the cross section of the specimen. This differential swelling will create a stress pattern consisting of a tension and a compression zone that will induce mechanosorption. This is something that is currently neglected by the FE model and will simplify the calculated displacement field.

3.3 Elastic modulus

The elastic moduli E_x, E_y and E_z obtained with compression tests on 36 specimens are visualised in Figure 7 for both relative humidity levels. See Figure 7f for an indication of the x, y and z direction in relation to the annual ring and fibre orientation. The size of the branches did not allow for a precise alignment with the local coordinate system. It should be noted that the principal z direction maintained in the current study aligns with the predominant local direction. The values of both the CW and OW sample sets are plotted against the measured MC and dry density. The mean value and standard deviation of the set's elastic moduli, dry density and MC are collected in Table 6.

At 44 % and 98 % RH, the mean E_z was 0.77 GPa and 0.71 GPa for CW, respectively, compared to 1.39 GPa and 0.92 GPa for OW. The mean E_z for CW is lower than that of OW, irrespective of the MC. For CW, a 23 % decrease in E_z was seen between 44 and 98 % RH, whereas for OW 44 %. The ratio between the E_z of CW and OW was 0.56 for 44 % RH and 0.77 for 98 % RH. The more prominent effect of MC on E_z of OW is reflected in this ratio. The lower E_z found for CW of stem is due to the larger microfibril angle of CW (Gindl 2002; Joffre et al. 2014; Kollmann and Côté 1968; Timell 1986a). For CW from stem, Timell (1986a) reported a longitudinal elastic modulus between 4.45 and 6.73 GPa and for NW between 10.56 and 12.56 GPa obtained for *Picea abies* tested in compression parallel to the grain, with ratios varying between 0.42 and 0.86. The values reported for E_z in the current study are smaller than those collected by Timell (1986a) for Norway spruce NW and CW from stem. This can be explained by the mechanical differences seen between stem and branch wood (Färber et al. 2001). For example, Timell (1986a) (page 576) reported an 11 % difference in longitudinal elastic modulus between stem (6.99 GPa) and branches (6.29 GPa) of American conifers. In addition, Gurau et al. (2008) reported a 428 % difference in modulus of elasticity between stem (11.20 GPa) and branches (2.12 GPa) of Scots pine. The research assigned the difference to the presence of juvenile wood, lower density then found in the stem, and compression wood. In addition, Färber et al. (2001) reported that the MFA for branches is generally larger than for stem wood of Norway spruce.

A mean value of 0.39 GPa is reported for E_x for OW at 44 % RH and 0.27 GPa at 98 % RH. For CW, these values are 0.42 and 0.33 GPa, respectively. The mean value of E_y is 0.26 GPa at 44 % RH and 0.20 GPa at 98 % RH for OW, and 0.38 and 0.34 GPa for CW, respectively. Since the principal global axes x and y do not align with the local cylindrical coordinate directions r and t, the elastic moduli, E_x and E_y, are both a combination of E_r and E_t. For Norway spruce NW, E_r tends to be larger than E_t (Keunecke et al. 2007). The elastic moduli related to the x direction presented in the current study are larger than those for the y direction, except for 98 % RH. This comes as a surprise, since the y direction is dominated by E_r. However, it should be noted that the standard deviation of E_x and E_y are relatively high. Keunecke et al. (2007) reported a mean value for E_r of 1.80 ± 0.01 GPa and a mean value for E_t of 1.18 ± 0.02 GPa. As seen for E_z, the values for E_y and E_x are much lower for branch wood then for stem wood. However, no values were found in literature to substantiate these finding. Both E_x and E_y for CW seem to be less affected by MC then OW. For E_x, a decrease of 32 % for OW was seen compared to 22 % for CW. For E_y, this decrease was 21 % for OW and 10 % for CW.

A linear relationship was established between elastic moduli and MC using Equations (7)–(10) for both OW and CW. These relations were established in the local coordinate system and incorporated into the FE model to simulate elastic behaviour. The results are visualised in Figure 7a–c and the constants needed to describe the relationship can be found in Table 7. The table also provides the goodness-of-fit (R^2) for each regression analysis. The R^2 values are quite low,

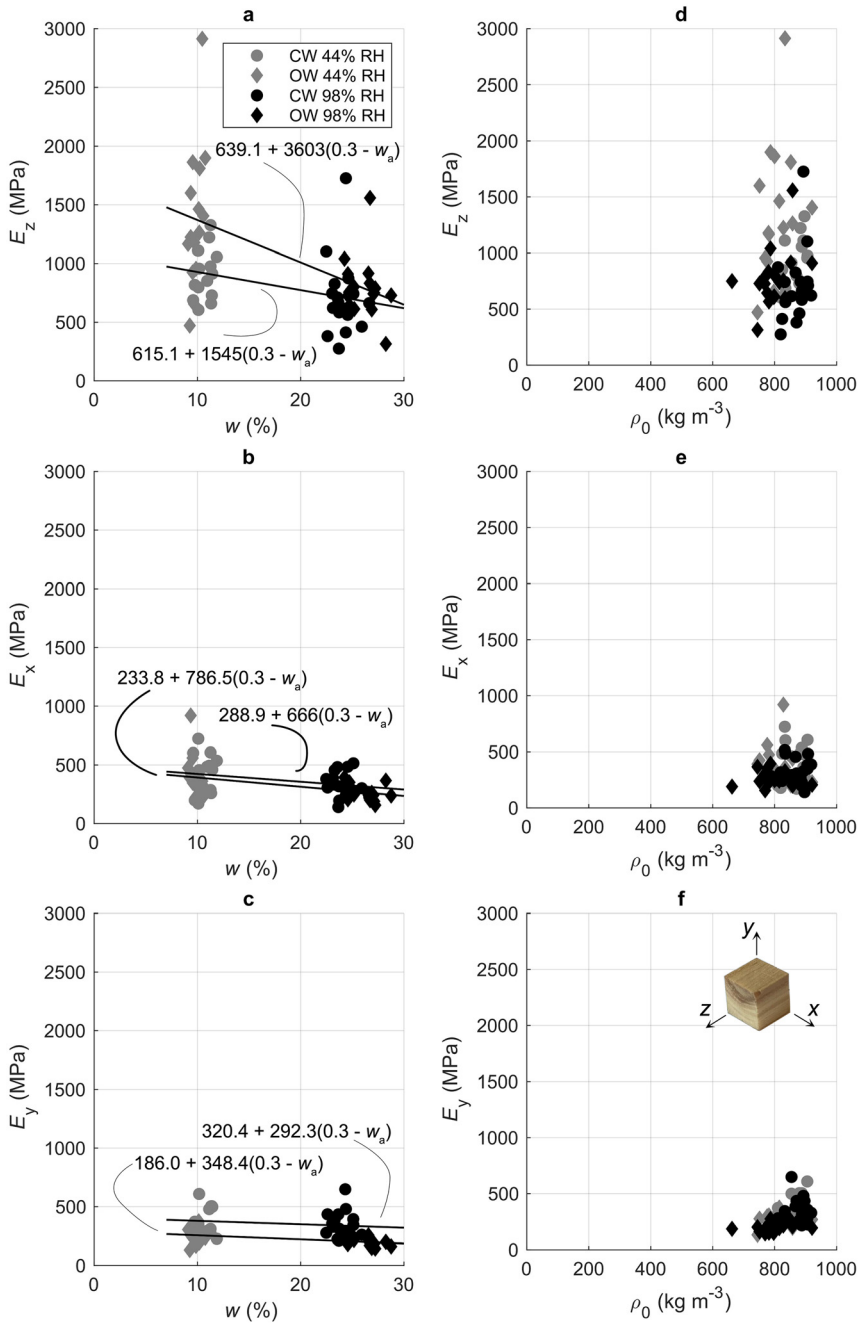

Figure 7: Relationship between elastic moduli, E, and moisture content, w, or dry density, ρ_0. CW indicates compression wood, OW indicates opposite wood, RH is relative humidity and w_a refers to the unitless moisture content below fibre saturation point.

which indicates that the results do not follow a linear trend. This can be due to – for example – a high quality variation of wood, a general scatter and the small size of the sample set. Similar relationships between elastic modulus and MC were given in Ormarsson et al. (1998) for Norway spruce NW, and show much higher values for E_l, E_r and E_t, than given in the present study. Other modelling parameters obtained from experimental data, such as MC, dimensions and pith location can be found in the SI section.

3.4 Dry density

The second column of Figure 7 shows that the measurements seem to follow the trend between elastic modulus and density predicted by Gibson and Ashby, that is linearly and cubically increasing stiffness with respect to density in the longitudinal and transverse directions, respectively (Gibson 2004). The average value and standard deviation of the dry-density sets can be found in Table 6. An average dry density

Table 6: Dry density, ρ_0, volumetric moisture content, w_i, and elastic moduli, E, related to x, y, and z testing directions for opposite wood (OW) and compression wood (CW) at 44 % and 98 % relative humidity, ϕ, including standard deviation (std).

	ρ_0 (kg/m^3)	w_i (%)		E_z (GPa)		E_x (GPa)		E_y (GPa)	
ϕ (%)	–	44	98	44	98	44	98	44	98
OW	796	9.3	26.3	1.39	0.77	0.39	0.27	0.26	0.20
Std	54	0.5	1.8	0.60	0.25	0.18	0.07	0.06	0.04
CW	871	10.6	24.1	0.92	0.71	0.42	0.33	0.38	0.34
Std	34	0.8	1.1	0.21	0.32	0.17	0.11	0.11	0.11

Table 7: Parameters obtained with regression analysis to describe the elastic moduli for opposite wood (OW) and compression wood (CW) using Equations (7)–(10), where R^2 indicates goodness-of-fit.

		$E_{l0}\cdot10^3$ (MPa)	$E_{lw}\cdot10^3$ (MPa)	R^2
OW	E_l (MPa)	0.64	3.60	0.32
	E_r (MPa)	0.23	0.79	0.22
	E_t (MPa)	0.19	0.35	0.27
CW	E_l (MPa)	0.62	1.55	0.13
	E_r (MPa)	0.29	0.67	0.10
	E_t (MPa)	0.32	0.29	0.03

w_f = 0.3 (–), T_0 = 20 °C, T = 21 °C.

of 871 kg m^{-3} is found for CW and 796 kg m^{-3} for OW, with a CW to OW ratio of 1.09. The values are higher than generally expected for NW. For example, Niemz and Sonderegger (2017) reported values between 370 and 540 kg m^{-3} for Norway spruce NW, where Boutelje and Rydell (1995) (page 27) mentioned values between 370 and 440 kg m^{-3}. The values reported in the current study also show higher values for CW than for OW, as would also be expected (Gardiner et al. 2014; Kollmann and Côté 1968; Timell 1986a). The cell walls of CW are significantly thicker than those of NW, dominating over the fact that the fraction of highly dense cellulose is lower in CW. Although values of dry density for branches is hard to find in literature, Timell (1986a) does mention CW to NW ratios between 1.1 and 1.8, which are almost in line with the value of 1.09 found in the current study. In addition, Li et al. (2014) reported an average dry density of 638 kg m^{-3} for CW found in a branch of Scots pine and 542 kg m^{-3} for the corresponding OW.

3.5 Moisture content

The MC determined for all specimens in the OW and CW sample sets are presented in the first column of Figure 7. The mean value and standard deviation of each set can be found in Table 6. The mean MC of OW was 9.33 % for a RH of 44 %. For the same RH, a mean MC of 10.56 % was found for CW. At 98 % RH, these values were 26.33 % and 24.12 %, respectively. These values lie around the ideal MC of 10 % (44 % RH) and 25 % (98 % RH) presented in previous section. No clear trends could be seen between CW and OW and no clear differences between NW, CW and OW are reported in literature. The differences in swelling is therefore not like to be due to more water in one type of wood, but rather a question of different structural reorganisation at molecular scale. Gardiner et al. (2014) do mention that the MC of green reaction wood is generally lower than that of NW and that the drying rate of CW is lower than that of NW.

4 Conclusions

The study showed that the recently developed XμCT aided FE methodology assisted in a considerate design and execution of the XμCT aided FE process of wood. Bottlenecks within and between each step of the process were also identified. The process and output could have benefitted from a CT scanner with a good control of thermal drift and artefacts. This would have led to tomograms with a better spatial and contrast resolution. An *in-situ* testing approach through a built-in climate chamber for the scanner would also have led to higher quality images and would have benefited the DVC analysis. The XμCT aided FE process was far from *automated*, which allowed for human-induced errors. In addition, the level of details adopted by the numerical model influenced the accuracy of the determined material properties. The study focused on a homogeneous cylindrically orthotropic model. A uniform density was assumed, no distinction was made between early, late and transition wood and a possible moisture gradient was neglected. These choices led to a simplified interpretation of radial and tangential hygroexpansion coefficients. The fact that these differences arise as a consequence of the model is interesting in itself and should be further investigated.

The recently developed XμCT aided FE methodology was tested on two specimens of Norway spruce from tree branches to determine the hygroexpansion coefficients of OW and CW. The small sample size did not justify the variability of material and therefore no statistically significant conclusions could be drawn from the results. Therefore, a summary is given here instead. The results showed that OW and CW hold a similar MC at specific RH levels and similar transverse hygroexpansion coefficients. On the other hand, CW has a higher density (871 kg m^{-3}) and longitudinal hygroexpansion coefficient (0.19) than OW (796 kg m^{-3}, –0.004), and the elastic moduli seem to be less affected by MC. These

differences are unlikely due to water in one type of wood, but rather a question of characteristics of the microstructure such as microfibril angle.

Author contributions: Conceptualization: Sara Florisson (SF), Kristofer Gamstedt (KG), Marie Hartwig (MH), Malin Wohlert (MW); methodology: SF, KG; software: SF; validation: SF; data curation: SF, MH; formal analysis: SF; investigation: SF, MH; resources: MH; writing – original draft: SF; writing, review & editing: SF, KG, MW, MH; visualization: SF; project administration: SF.

Conflict of interest statement: On behalf of all authors, the corresponding author states that there is no conflict of interest regarding this article.

Research funding: Not applicable.

Data availability: Not applicable.

Code availability: Not applicable.

References

Auenhammer, R.M., Mikkelsen, L.P., Asp, L.E., and Blinzler, B.J. (2021). Automated X-ray computed tomography segmentation method for finite element analysis of non-crimp fabric reinforced composites. Compos. Struct. 256: 113136.

Auenhammer, R.M., Jeppesen, N., Mikkelsen, L.P., Dahl, V.A., Blinzler, B.J., and Asp, L.E. (2022). Robust numerical analysis of fibrous composites from X-ray computed tomography image data enabling low resolutions. Compos. Sci. Technol. 224: 109458.

AVIZO (2021). User's guide Avizo 3D 2021–2. Thermo Fischer Scientific, Waltham, Massachusetts, USA.

Badel, E. and Perre, P. (2001). Using a digital X-ray imaging device to measure the swelling coefficients of a group of wood cells. Non Destr. Test. Eval. Int. 34: 345–353.

Bay, B.K., Smith, T.S., Fyhrie, D.P., and Saad, M. (1999). Digital volume correlation: three dimensional strain mapping using X-ray tomography. Exp. Mech. 39: 217–226.

Boutelje, J.B. and Rydell, R. (1995). *Träfakta: 44 träslag i ord och bild (Tree facts: 44 wood species in word and pictures) (Swedish)*. Trätek, Stockholm, Sweden.

Buljac, A., Jailin, C., Mendoza, A., Neggers, J., Taillandier-Thomas, T., Bouterf, A., Smaniotto, B., Hild, F., and Roux, S. (2018). Digital volume correlation: review of progress and challenges. Exp. Mech. 58: 661–708.

Burgert, I., Frühmann, K., Keckes, J., Fratzl, P., and Stanzl-Tschegg, S. (2004). Structure-function relationships of four compression wood types: micromechanical properties at the tissue and fibre level. Trees 18: 480–485.

Burgert, I., Eder, M., Gierlinger, N., and Fratzl, P. (2007). Tensile and compressive stresses in tracheids are induced by swelling based on geometrical constraints of the wood cell. Planta 226: 981–987.

da Silva Moreira, L., Lima, J.T., Dias Soares, B.C., and Pereira Moutinho, V.H. (2023). Wood quality of residual branches of *Hymenaea courbaril* L. from logging in the Amazon rainforest. Holzforschung 77: 16–27.

du Plessis, A., Tshibalanganda, M., and le Roux, S.G. (2020). Not all scans are equal: X-ray tomography image quality evaluation. Mater. Today Commun. 22: 100792.

European Committee for Standardization (2003). *Moisture content of a piece of sawn timber – Part 1: determination by oven dry method*. EN 13183-1, Brussels, Belgium.

Florisson, S. and Gamstedt, E.K. (unpublished data). An overview of lab-based microscopic computed tomography aided finite element modelling of wood and its current bottlenecks. Treesearch, Stockholm.

Florisson, S., Vessby, J., and Ormarsson, S. (2021). A three-dimensional numerical analysis of moisture flow in wood and of the wood's hygro-mechanical and visco-elastic behaviour. Wood Sci. Technol. 55: 1269–1304.

Florisson, S. (2022). A methodology for microscopic computed tomography aided finite element modelling of wood. In: *Conference proceedings of the 27th Swedish Mechanics Days (Svenska Mekanikdagar), 2022*. Luleå University of Technology, Luleå, Sweden.

Forsberg, F., Sjödahl, M., Mooser, R., Hack, E., and Wyss, P. (2010). Full three-dimensional strain measurements on wood exposed to three-point bending: analysis by use of digital volume correlation applied to synchrotron radiation micro-computed tomography image data. Strain 46: 47–60.

Fortino, S., Sippola, M., Andersson, T., Immonen, K., Miettinen, A., and Hradil, P. (2017). X-ray mico-tomography based FEM modelling of hygroexpansion in PLA composites reinforced with birch pulp fibers. Rakenteiden Mekaniikka 50: 131–136.

Färber, J., Lichtenegger, H.C., Reiterer, A., Stanzl-Tschegg, S., and Fratzl, P. (2001). Cellulose microfibril angles in a spruce branch and mechanical implications. J. Mater. Sci. 36: 5087–5092.

Gardiner, B., Barnett, J., Saranpää, P., and Gril, J. (2014). *The biology of reaction wood*. Springer Series in Wood Science, Berlin, Germany.

Gibson, L.J. (2004). Biomechanics of cellular solids. J. Biomech. 38: 377–399.

Gindl, W. (2002). Comparing mechanical properties of normal and compression wood in Norway spruce: the role of lignin in compression parallel to the grain. Holzforschung 50: 395–401.

Gonçalves, R., Garcia, G.H.L., Brazolin, S., Bertoldo, C., and Ruy, M. (2019). Methodology for the characterization of elastic constants of wood from tree branches. Bioresources 14: 8439–8454.

Groover, A. (2016). Gravitropism and reaction woods of forest trees – evolution, functions and mechanisms. New Phytol. 211: 790–802.

Guo, P., Zhao, X., Feng, Q., and Yang, Y. (2023). Branchwood properties of two *Tilia* species collected from natural secondary forests in Northeastern China. Forests 14: 760.

Gurau, L., Cionca, M., Mansfield-Williams, H., Sawyer, G., and Zeleniuc, O. (2008). Comparison of the mechanical properties of branches and stem wood for three species. Wood Fiber Sci. 40: 647–656.

Hachem, C.E., Abahri, K., Vicente, J., Bennacer, R., and Belarbi, R. (2018). Hygromorphic characterization of softwood under high resolution X-ray tomography for hygrothermal simulation. Int. J. Heat Mass Transf. 54: 2761–2769.

Hartig, J.H., Bieberle, A., Engmann, C., and Haller, P. (2021). Voxel-based finite element modelling of wood elements based on spatial density and geometry data using computed tomography. Holzforschung 75: 742–753.

Hartwig, M. and Gamstedt, E.K. (2020). On the composite design of wood branches leading to improved bending strength. In: *IOP Conference Series: Materials Science and Engineering 2020*. Risø, Denmark, p. 012008.

Hild, F., Bouterf, A., Chamoin, L., Leclerc, H., Mathieu, F., Neggers, J., Pled, F., Tomicevic, Z., and Roux, S. (2016). Toward 4D mechanical correlation. Adv. Model. Simul. Eng. Sci. 3: 17.

Huber, J.A.J., Broman, O., Ekevad, M., Oja, J., and Hansson, L. (2022). A method for generating finite element models of wood boards from X-ray computed tomography scans. Comput. Struct. 260: 106702.

Joffre, T., Neagu, R.C., Bardage, S.L., and Gamstedt, K.E. (2014). Modelling of the hygroelastic behaviour of normal and compression wood tracheids. J. Struct. Biol. 185: 89–98.

Kamke, F.A., Nairn, J.A., Muszynski, L., Paris, J.L., Schwarzkopf, M., and Xiao, X. (2014). Methodology for micromechanical analysis of wood adhesive bonds using X-ray computed tomography and numerical modeling. Wood Fiber Sci. 46: 15–28.

Keunecke, D., Sonderegger, W., Pereteanu, K., Lüthi, T., and Niemz, P. (2007). Determination of Young's and shear moduli of common yew and Norway spruce by means of ultrasonic waves. Wood Sci. Technol. 41: 309–327.

Keunecke, D., Novosseletz, K., Lanvermann, C., Mannes, D., and Niemz, P. (2012). Combination of X-ray and digital image correlation for the analysis of moisture-induced strain in wood: opportunities and challenges. Eur. J. Wood Wood Prod. 70: 407–413.

Keyak, J.H., Meagher, J.M., Skinner, H.B., and Mote, C.D., Jr. (1990). Automated three-dimensional finite element modelling of bone: a new method. J. Biomed. Eng. 12: 389–397.

Keyak, J.H., Rossi, S.A., Jones, K.A., and Skinner, H.B. (1998). Prediction of femoral fracture load using automated finite element modeling. J. Biomech. 31: 125–133.

Kollmann, F.F.P. and Côté, W.A. (1968). *Principles of wood science and technology Part I: solid wood*. Springer-Verlag, Berlin/Heidelberg.

Lanvermann, C., Wittel, F.K., and Niemz, P. (2014). Full-field moisture induced deformation in Norway spruce: intra-ring variation of transverse swelling. Eur. J. Wood Wood Prod. 72: 43–52.

Li, X., Evans, R., Gapare, W., Yang, X., and Wu, H.X. (2014). Characterizing compression wood formed in Radiata pine branches. IAWA J. 35: 385–394.

Limodin, N., Réthoré, J., Adrien, J., Buffière, J.-Y., Hild, F., and Roux, S. (2011). Analysis and artifact correction for volume correlation measurements using tomographic images from a laboratory X-ray source. Exp. Mech. 51: 959–970.

Madi, K., Tozzi, G., Zhang, Q.H., Tong, J., Cossey, A., Au, A., Hollis, D., and Hild, F. (2013). Computation of full-field displacement in a scaffold implant using digital volume correlation and finite element analysis. Med. Eng. Phys. 35: 1298–1312.

Marasigan, O.S., Razal, R.A., Carandang, W.M., and Alipon, M.A. (2022). Physical and mechanical properties of stems and branches of Falcata [*Falcataria moluccana* (Miq.) Barneby & J.W. Grimes] Grown in Caraga, Philippines. Philipp. J. Sci. 151: 575–586.

Müller, U., Gindl, W., and Jeronimidis, G. (2006). Biomechanics of a branch – stem junction in softwood. Trees 20: 643–648.

Nanayakkara, B., Manley-Harris, M., Suckling, I.D., and Donaldson, L.A. (2009). Quantitative chemical indicators to assess the gradation of compression wood. Holzforschung 63: 431–439.

Niemz, P. and Sonderegger, W. (2017). *Holzphysik: Physik des Holzes und der Holzwerkstoffe (Wood physics: physics of wood and wood-based products) (in German)*. Carl Hanser Verlag, München, Germany.

Olarescu, A.M., Lunguleasa, A., and Radulescu, L. (2022). Using deciduous branch wood and conifer spindle wood to manufacture panels with transverse structure. Bioresources 17: 644–6463.

Ormarsson, S. (1999). *Numerical analysis of moisture related distortion in sawn timber*, Doctoral thesis. Department of Structural Mechanics, Chalmers University of Technology, Gothenburg, Sweden.

Ormarsson, S., Dahlblom, O., and Petersson, H. (1998). A numerical study of the shape stability of sawn timber subjected to moisture variation Part 1: theory. Wood Sci. Technol. 32: 325–334.

Patera, A., Carl, S., Stampanoni, M., Derome, D., and Carmeliet, J. (2018). A non-rigid registration method for the analysis of local deformations in the wood cell wall. Adv. Struct. Chem. Imag. 4: 1.

Perstorper, M., Johansson, M., Kliger, R., and Johansson, G. (2001). Distortion of Norway spruce timber: part 1. Variation of relevant wood properties. Eur. J. Wood Prod. 59: 94–103.

Simpson, W.T. (1971). Equilibrium moisture content prediction for wood. For. Prod. J. 21: 48–49.

SIMULIA (2017a). *Abaqus user subroutines guide*. Dassault Systèmes, Vélizy-Villacoublay, France.

SIMULIA (2017b). *Abaqus/CAE user's guide*. Dassault Systèmes, Vélizy-Villacoublay, France.

SkyScan (2011). *NRecon user manual*. SkyScan N.V., Brussels, Belgium.

Stanzl-Tschegg, S., Keunecke, D., and Tschegg, E.K. (2011). Fracture tolerance of reaction wood (yew and spruce wood in the TR crack propagation system). J. Mech. Behav. Biomed. Mater. 4: 688–698.

Timell, T.E. (1986a). *Compression wood in gymnosperms. Part 1: bibliography, historical background, determination, structure, chemistry, topochemistry, physical properties, origin, and formation of compression wood*. Springer, Berlin, Heidelberg.

Timell, T.E. (1986b). *Compression wood in gymnosperms. Part 2: Occurrence of stem, branch and root compression woods, factors causing formation of compression wood, gravitropism and compression wood, physiology of compression wood formation, inheritance of compression wood*. Springer, Berlin, Heidelberg.

Timell, T.E. (1986c). *Compression wood in gymnosperms. Part 3: ecology of compression wood formation, silviculture and compression wood, mechanism of compression wood action, compression wood in the lumber and pulp and paper industries, compression wood induced by the balsam woolly aphid, opposite wood*. Springer, Berlin, Heidelberg.

Wang, B., Pan, B., Tao, R., and Lubineau, G. (2017). Systematic errors in digital volume correlation due to the self-heating effect of a laboratory X-ray CT scanner. Meas. Sci. Technol. 28: 055402.

Withers, P.J., Bouman, C., Carmignato, S., Cnudde, V., Grimaldi, D., Hagen, C.K., Maire, E., Manley, M., Du Plessis, A., and Stock, S.R. (2021). X-ray computed tomography. Nat. Rev. 1: 18.

Włoch, W. (1975). Longitudinal shrinkage of compression wood in dependence on water content and cell wall structure. Acta Soc. Bot. Pol. XLIV: 217–229.

Zhang, M., Chavan, R.R., Smith, B.G., McArdle, B.H., and Harris, P.J. (2016). Tracheid cell-wall structures and locations of (1 → 4)-β-D-galactans and (1 → 3)-β-Dglucans in compression woods of radiata pine (Pinus radiata D. Don). BMC Plant Biol. 16: 194.

Zwanenburg, E.A., Williams, M.A., and Warnett, J.M. (2022). Review of high-speed imaging with lab-based x-ray computed tomography. Meas. Sci. Technol. 33: 012003.

Supplementary Material: This article contains supplementary material (https://doi.org/10.1515/hf-2023-0014).